

Box enhanced Charged Lepton Flavor Violation in the Grimus-Neufeld model

Vytautas Dūdėnas^{1,*}, Thomas Gajdosik^{1,†}, Uladzimir Khasianeovich^{2,‡},
Wojciech Kotlarski^{3,§} and Dominik Stöckinger^{2,¶}

¹*Institute of Theoretical Physics and Astronomy, Faculty of Physics,
Vilnius University, 9 Saultėkio, LT-10222 Vilnius, Lithuania*

²*Institut für Kern- und Teilchenphysik, TU Dresden, Zellescher Weg 19, 01069 Dresden, Germany*

³*National Centre for Nuclear Research, Pasteura 7, 02-093 Warsaw, Poland*

In the Grimus-Neufeld model (GNM) the neutrino mass generation from an extended Higgs sector leads to bounds for Charged Lepton Flavour Violating (cLFV) processes. Here we update bounds from a previous study by extending the parameter space to a nonvanishing Majorana phase of the Pontecorvo-Maki-Nakagawa-Sakata matrix and to heavier charged Higgs boson masses. Three-body cLFV decays are shown to contribute significantly in the large mass regions, as the boxes are enhanced relatively to photonic diagrams. This is in contrast to the smaller mass region studied before, in which the two-body decays tightly restrict the parameter space. The Majorana phase is shown to change limits within one order of magnitude. The tiny seesaw scale is assumed, which makes the cLFV decays in the GNM similar to the cLFV decays in the scotogenic model and the scoto-seesaw models.

I. INTRODUCTION

The smallness and hierarchies of neutrino masses might be explained in models featuring radiative mass generation. Three simple examples are provided by the scotogenic model [1], the scoto-seesaw model [2] and the Grimus-Neufeld model (GNM) [3]. Specifically the GNM is an economical model with only one single sterile neutrino N and the extended scalar sector of the two-Higgs-doublet model (2HDM). At tree level, the seesaw mechanism generates only a single non-vanishing neutrino mass, governed by a Z_2 -odd effective Yukawa coupling y ; at the one-loop level, loops involving the extra Higgs states generate a second non-vanishing neutrino mass, governed by the Peccei-Quinn symmetry breaking Higgs potential parameter λ_5 . An appealing parameter region of the GNM studied in Refs. [4, 5] is the “tiny” seesaw scale region, where the sterile Majorana mass is below the electroweak scale and the Peccei-Quinn and Z_2 breaking parameters are small.

In neutrino mass models such as the GNM or the scotogenic or scoto-seesaw models, the neutrino mass generation automatically also implies the existence of Charged Lepton Flavour Violation (cLFV) processes, studied in [2, 6–8] for high sterile neutrino masses. In fact, in the three mentioned models, the predictions for cLFV processes become similar (or even identical, for the scoto-seesaw and GNM models) in the case of a tiny sterile neutrino mass, as discussed in [5], thus our study also complements the ones in [2, 6–8].

In Ref. [5], the interplay between the neutrino sector,

the scalar sector and cLFV was used to analyze which restrictions are imposed by cLFV on the scalar sector. A main finding was that a single parameter combination, called photon factor, is constrained by cLFV, if the charged Higgs mass is sufficiently small (less than 1 TeV). In most of the parameter space, the decay $\mu \rightarrow e\gamma$ was most constraining, but in order to obtain absolute, most conservative bounds, special parameter regions needed to be considered in which $\tau \rightarrow e\gamma$ or $\tau \rightarrow \mu\gamma$ were important.

Ref. [5] focused on the tiny seesaw scale region of the GNM, but several additional restrictions on the parameter regions were imposed in order to simplify the analysis. The mass of the charged Higgs was constrained to be less than 1 TeV and the free Majorana phase was set to zero. In the present paper we relax those restrictions and complete the phenomenological study of this GNM scenario in the tiny seesaw scale, by studying the effects of the free Majorana phase and including large values of the charged Higgs mass. A major implication of the extended parameter space is that further decays such as $\tau \rightarrow 3e$ and $\tau \rightarrow 3\mu$ need to be considered because the related box diagram contributions can now be significant.

In section II we provide a more detailed summary of the GNM and of the main findings of Ref. [5]. We also provide an overview of the changes in the considered parameter space and the expected effects. Section III is devoted to the extended phenomenological analysis, and section IV presents our conclusions.

II. THE MODEL AND ITS PARAMETERS

We will briefly describe the main features of the GNM to introduce our definitions. For a more detailed explanation of the model we refer to [5].

The GNM consists of the general 2HDM with an added gauge singlet Weyl fermion N with a Majorana mass M , called the sterile neutrino. This allows for an additional

* vytautasdudenas@inbox.lt

† thomas.gajdosik@ff.vu.lt

‡ uladzimir.khasianeovich@tu-dresden.de

§ wojciech.kotlarski@ncbj.gov.pl

¶ dominik.stoekinger@tu-dresden.de

Yukawa coupling with the singlet N . New terms to the 2HDM Lagrangian read as:

$$\mathcal{L} \ni -\frac{1}{2}MNN - Y_j^{(i)}\ell_j\epsilon H_i N + h.c. \quad (1)$$

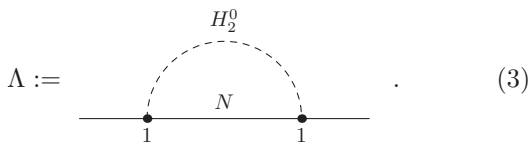
The matrix $\epsilon = i\sigma_2$ combines the two doublets to an $SU(2)$ invariant product, i is the Higgs family index, while j is the flavor index. We can always use the Higgs basis, where the Yukawa coupling $Y^{(1)}$ to the Higgs doublet with non-vanishing vacuum expectation value (VEV) enables the seesaw mechanism, while $Y^{(2)}$ leads to radiative neutrino mass generation for light neutrinos, resulting in two non-vanishing light neutrino masses at one-loop.

We assume an approximate Z_2 symmetry, under which H_2 is odd and H_1 is even. The Yukawa coupling $Y^{(1)}$ then explicitly breaks this symmetry by a tiny amount. To reproduce the light neutrino masses at an eV scale with a seesaw mechanism, one then must have a tiny mass for the sterile neutrino. We call this the ‘‘tiny’’ seesaw scale and assume:

$$M \approx m_4 < 10 \text{ GeV} \Leftrightarrow \sum_i |Y_i^{(1)}|^2 < 10^{-14}, \quad (2)$$

where m_4 is the pole mass of the sterile neutrino. This makes $Y_i^{(1)}$ to be at least an order of magnitude smaller than the electron Yukawa coupling of the SM. In the general 2HDM the Yukawa interactions of charged leptons with H_2 would also break the Z_2 symmetry, thus we set them to zero.

The parameter that is responsible for radiative mass generation, and thus relates the scalar and neutrino sectors, can be defined via the neutrino self energy diagram at vanishing external momentum:



In the loop, H_2^0 is the neutral component of the second

Higgs doublet in the Higgs basis and N is the sterile neutrino. As indicated, the coupling values have been normalized to unity such that Λ essentially corresponds to the mass-dependent loop function. For the inert-like scalar sector and the tiny seesaw scenario, this parameter reduces to

$$\Lambda = \frac{m_4}{32\pi^2} \ln \left(\frac{m_H^2}{m_A^2} \right), \quad m_4 \ll v, \quad (4)$$

where m_4 is the mass of the sterile neutrino and $m_{H,A}$ are the masses of the extra neutral CP-even/odd Higgs bosons. We note, however, that our results on cLFV directly apply for the most general scalar potential, using the definition of Eq. (3).

In the tiny seesaw limit we are able to get the one-loop parameterization of Yukawa couplings $Y^{(i)}$, which automatically reproduce the observed Pontecorvo-Maki-Nakagawa-Sakata (PMNS) matrix and the neutrino mass differences squared [5]. For cLFV rates, the Yukawa coupling of neutrinos to the first Higgs doublet in the Higgs basis can be neglected [5] and thus only the Yukawa coupling to the second Higgs doublet is important for us, which is:

$$Y^{(2)} \equiv \text{sign}(\Lambda) \sqrt{\frac{m_2^{\text{pole}}}{|z\Lambda|}} \begin{bmatrix} 0 \\ \cos r e^{i\omega_{22}} \\ \sin r e^{i\omega_{32}} \end{bmatrix}^T U, \quad (5)$$

$$\omega_{32} \equiv -\frac{1}{2} \arcsin \left(\frac{\sin(2\omega_{22})}{t_{32} \tan^2 r} \right), \quad t_{32} \equiv \frac{m_3^{\text{pole}}}{m_2^{\text{pole}}}, \quad (6)$$

$$z = z(r, \omega_{22}) \equiv \cos^2 r e^{2i\omega_{22}} + t_{32} \sin^2 r e^{2i\omega_{32}}, \quad (7)$$

where the neutrino masses m_2^{pole} , m_3^{pole} , and the mixing matrix U , have different values for Normal ordering (NO) and Inverted ordering (IO) and are related to the experimental values [9] as in table I, where the matrix O_{IO} relates our mixing matrix convention to the usual 3ν convention, used in Ref. [9], in the IO case:

$$O_{\text{IO}} = \begin{pmatrix} 0 & 1 \\ \mathbb{1}_{2 \times 2} & 0 \end{pmatrix}. \quad (8)$$

The PMNS matrix is defined as [9]:

$$U_{\text{PMNS}} = \begin{pmatrix} 1 & 0 & 0 \\ 0 & c_{23} & s_{23} \\ 0 & -s_{23} & c_{23} \end{pmatrix} \begin{pmatrix} c_{13} & 0 & s_{13} e^{-i\delta_{\text{CP}}} \\ 0 & 1 & 0 \\ -s_{13} e^{i\delta_{\text{CP}}} & 0 & c_{13} \end{pmatrix} \begin{pmatrix} c_{12} & s_{12} & 0 \\ -s_{12} & c_{12} & 0 \\ 0 & 0 & 1 \end{pmatrix} \begin{pmatrix} e^{i\eta_1} & 0 & 0 \\ 0 & e^{i\eta_2} & 0 \\ 0 & 0 & 1 \end{pmatrix}, \quad (9)$$

where η_1 and η_2 are unknown Majorana phases, and $s_{ij} = \sin \theta_{ij}$, and $c_{ij} = \cos \theta_{ij}$.

While the parameters r and ω_{22} are free, not all values reproduce neutrino masses and mixings. They are

restricted by $z \in \mathbb{R}$ (see [5]). Λ enters as a free parameter in Eq. (5). Every other parameter is to be determined by the neutrino masses and mixings. However, the Majorana phases η_1 and η_2 are not observed so far and thus

	m_2^{pole}	m_3^{pole}	U
NO	$\sqrt{\Delta m_{21}^2}$	$\sqrt{ \Delta m_{32}^2 + \Delta m_{21}^2}$	U_{PMNS}^\dagger
IO	$\sqrt{ \Delta m_{32}^2 - \Delta m_{21}^2}$	$\sqrt{ \Delta m_{32}^2 }$	$O_{\text{IO}} U_{\text{PMNS}}^\dagger$

TABLE I. Relations of neutrino pole masses and mixings, to the oscillations parameters for NO and IO.

are, in principle, free parameters. In the GNM, η_1 is absorbed into the field redefinition and has no physical significance. This is the direct consequence of the lightest neutrino being massless in the GNM: a massless neutrino simply does not have a Majorana phase, and hence $\eta_1 = 0$. The Majorana phase η_2 , however, is a free parameter in the GNM that does have a physical significance. Thus the free parameters that parameterize $Y^{(2)}$ are:

$$r, \quad \omega_{32}, \quad \Lambda, \quad \eta_2. \quad (10)$$

Note that to simplify the study in [5], we set $\eta_2 = 0$. We now relax this assumption and study its significance for the bounds drawn from cLFV decays.

The Yukawa coupling $Y^{(2)}$ leads to one-loop generated cLFV decays with a charged Higgs boson and sterile neutrino in the loop. These amplitudes for $\ell_i \rightarrow \ell_j \gamma$ and $\ell_i \rightarrow \ell_j \ell_k \ell_k$ consist of penguin and box contributions, which are [5]:

$$A_{\text{penguin}} \sim \frac{Y_i^{(2)*} Y_j^{(2)}}{m_{H^\pm}^2} \sim \frac{1}{|\Lambda| m_{H^\pm}^2}, \quad (11)$$

$$A_{\text{box}} \sim \frac{Y_i^{(2)*} Y_j^{(2)} |Y_k^{(2)}|^2}{m_{H^\pm}^2} \sim \frac{1}{\Lambda^2 m_{H^\pm}^2}, \quad (12)$$

where we used the parameterization from Eq. (5) to factor out the so-called *photon factor* $|\Lambda| m_{H^\pm}^2$ and the *box factor* $\Lambda^2 m_{H^\pm}^2$.

It is then useful to translate the set of free parameters of Eq. (10), together with the free mass of the charged Higgs m_{H^\pm} into the new set of parameters

$$r, \quad \omega_{32}, \quad \eta_2, \quad |\Lambda| m_{H^\pm}^2, \quad \Lambda^2 m_{H^\pm}^2 \quad (13)$$

that directly controls the cLFV rates.

In the tiny-seesaw parameter region, the cLFV decays thus dominantly depend on five parameters, Eq. (13). Two of them, $|\Lambda| m_{H^\pm}^2$ with $\Lambda^2 m_{H^\pm}^2$, are connected to the Higgs sector while others parameterize the Yukawa sector only.

A. Recap of the previous study

In [5] we assumed a relatively low charged Higgs mass of $m_{H^\pm} \lesssim 1$ TeV and $\eta_2 = 0$. This led to a suppression of box diagrams, which are essentially governed by the factor $\Lambda^2 m_{H^\pm}^2$, called box factor. In addition, three-body

Process	Current phase	Next phase
$\mu \rightarrow e \gamma$	MEG [10]: $4.2 \cdot 10^{-13}$	MEG-II [11]: $6 \cdot 10^{-14}$
$\tau \rightarrow e \gamma$	BaBar [12]: $3.3 \cdot 10^{-8}$	Belle-II [13]: $3.0 \cdot 10^{-9}$
$\tau \rightarrow \mu \gamma$	BaBar [12]: $4.5 \cdot 10^{-8}$	Belle-II [13]: $1.0 \cdot 10^{-9}$
$\mu \rightarrow 3e$	SINDRUM [14]: $1 \cdot 10^{-12}$	Mu3e-I [15]: $2 \cdot 10^{-15}$
$\tau \rightarrow 3e$	Belle-I [16]: $2.7 \cdot 10^{-8}$	Belle-II [13]: $4.6 \cdot 10^{-10}$
$\tau \rightarrow \mu e e$	Belle-I [16]: $1.8 \cdot 10^{-8}$	Belle-II [13]: $3.1 \cdot 10^{-10}$
$\tau \rightarrow e \mu \mu$	Belle-I [16]: $2.7 \cdot 10^{-8}$	Belle-II [13]: $4.6 \cdot 10^{-10}$
$\tau \rightarrow 3\mu$	Belle-I [16]: $2.1 \cdot 10^{-8}$	Belle-II [13]: $3.6 \cdot 10^{-10}$

TABLE II. Current and next experimental bounds, divided into different phases, related to corresponding observables. Data for τ decays for Belle-II was obtained from the figure 189 of Ref. [13].

decays turned out to be unimportant in that parameter region. Instead, two-body decays gave the strongest constraints. As a result, only three out of the five parameters in Eq. (13) were important, and we could put an experimental bound on the photon factor $|\Lambda| m_{H^\pm}^2$ as a function of the $\omega_{22} - r$ plane from two-body decays only. The used branching ratios are listed in table II. They are categorized by *phases* of experiments: the current experimental limits are referred as *current phase*, while *next phase* are the planned sensitivities of the upgraded experiments.

The most constraining experiment for the photon factor in almost all the $\omega_{22} - r$ plane is $\mu \rightarrow e \gamma$. However, there exist fine-tuned areas, in which this decay rate vanishes, because of the vanishing of either $Y_e^{(2)}$ or $Y_\mu^{(2)}$. The point in the $\omega_{22} - r$ plane where the corresponding Yukawa coupling $Y_{e,\mu}^{(2)}$ vanishes (and thus, the corresponding decay rate) one gets [5] from Eq. (5):

$$\cot(r) e^{i(\omega_{22} - \omega_{32})} = -t_{32} \frac{U_{3f}}{U_{2f}} \quad (14)$$

for flavor $f = e, \mu$. There is one solution of Eq. (14) for each flavour. This means that there are only two special regions in which $\mu \rightarrow e \gamma$ and $\mu \rightarrow 3e$ decays are suppressed: around the points in the $\omega_{22} - r$ plane with $Y_{e,\mu}^{(2)} = 0$.

In these special regions, the τ decay experiments give stronger constraints than μ decays. The experimental sensitivities of τ decays (table II) give much weaker constraints on the photon factor. This also means that in most of the $\omega_{22} - r$ plane, i.e. outside the special regions, an observation of τ decays in the experiments with the planned sensitivities of next phase experiments (second row of table II) is already excluded by $\mu \rightarrow e \gamma$ in the current phase.

Thus, to specify the regions in a robust way, we define *special regions* as the regions in the $\omega_{22} - r$ plane where the two-body decays of τ lepton are potentially observable at the Belle-II experiment. In short, the regions are defined by the following inequalities for the theory

Parameters studied in [5]	Current parameters
$\eta_2 = 0$	$-\pi < \eta_2 < \pi$
$m_{H^\pm} < 1 \text{ TeV}$	$m_{H^\pm} < 5 \text{ TeV}$
$ z > 0.5$	$ z > 0.38$
$ Y_i^{(2)} < 1$	$\sum_i Y_i^{(2)} ^2 < 8\pi$

TABLE III. Extensions of parameter ranges, compared to the values studied in [5].

predictions for μ and τ decays:

special region 1:

$$\begin{aligned} \text{BR}(\text{Belle-II}) < \text{BR}(\tau \rightarrow e\gamma) < \text{BR}(\text{BaBar}) \\ \text{while } \text{BR}(\mu \rightarrow e\gamma) < \text{BR}(\text{MEG}), \end{aligned} \quad (15)$$

special region 2:

$$\begin{aligned} \text{BR}(\text{Belle-II}) < \text{BR}(\tau \rightarrow \mu\gamma) < \text{BR}(\text{BaBar}) \\ \text{while } \text{BR}(\mu \rightarrow e\gamma) < \text{BR}(\text{MEG}), \end{aligned}$$

where by BR(experiment) we indicate the expected (for Belle-II) or current (MEG and BaBar) limits on the branching ratio of a corresponding decay in the experiment. They occupy relatively small areas in the $\omega_{22} - r$ plane, as one sees in figure 7 of [5] and thus these areas can be dubbed as “unnatural”/fine-tuned.

The *absolute* lower bound on the photon factor is defined as the lowest photon factor possible anywhere in the $\omega_{22} - r$ plane, for which all the experimental constraints, shown in table II are satisfied. Naturally, this absolute bound is defined by the limits on the branching ratios of τ decays in the special regions, as they are the weakest possible constraints. However, since the special regions might be seen as unnatural, we also define a *typical* bound on the photon factor, which is the bound got in the same way, but excluding the special regions and thus derived from $\mu \rightarrow e\gamma$ branching ratio.

From a practical point of view, the typical bound should coincide with the bound from the rough random scan over the $\omega_{22} - r$ plane. In contrast, to derive the absolute bound, one has to use the analytic solution of (14), to get the point in the $\omega_{22} - r$ plane of $\mu \rightarrow e\gamma$ close to zero to a high degree of accuracy. As a result, the typical bound is $O(10^2)$ stronger than the absolute one.

B. Extending the parameter space

The extension of the parameter space in the current study vs. the study of [5] is summarized in table III. Here we briefly discuss the expected effects and related subtleties.

The extension of η_2 is rather straightforward and allows to study the η_2 dependence of the limits. We expect the qualitative behavior of the model to remain unchanged and expect the resulting limits to stay within the same order of magnitude. For the IO, however, it

turns out that some values of η_2 push the special regions into the area that we previously excluded in the study due to a too large tree-loop cancellation in the neutrino pole mass calculation. This cancellation is encoded in the parameter z of Eq. (7), which can be shown to be [5]:

$$|z| = \frac{m_3^{\text{pole}}}{m_3^{\text{tree}}}, \quad (16)$$

where m_3^{tree} is the tree-level neutrino mass. Hence we decided to extend the considered values of z to allow roughly 62% cancellation instead of 50% to incorporate the special regions for all η_2 .

In the parameter regions where m_{H^\pm} is large, larger Yukawa couplings are allowed. As a result, box diagram contributions governed by four powers of Yukawa couplings can become relevant. To see this, consider a fixed $|\Lambda|m_{H^\pm}^2$ (which is fixed by the limits of the two-body decay experiments) and put it into Eqs. (11, 12) to verify the following proportionality of the relative importance of box diagrams:

$$A_{\text{box}}/A_{\text{penguin}} \sim 1/\Lambda \stackrel{|\Lambda|m_{H^\pm}^2=\text{const}}{\sim} m_{H^\pm}^2. \quad (17)$$

Hence extending the mass range for m_{H^\pm} also increases the importance of three-body decays. At some very large m_{H^\pm} , however, limits drawn from perturbative unitarity will become more important than the limits drawn from cLFV decays.

The restriction of Yukawa coupling values in Ref. [5] was technically motivated by the numerical stability of the neutrino pole mass calculation in FlexibleSUSY [17–19], which also served as a rigorous numerical check of the parameterization of Eq. (5). This restriction, even though somewhat ad hoc, was of little consequence since it was in general weaker than the ones derived from cLFV in low m_{H^\pm} region, thus it did not affect our results drawn from two-body decays. We now look at larger m_{H^\pm} , drop the ad hoc restriction on the Yukawa coupling, and only apply the looser restriction derived from perturbative unitarity (see section II C). For $m_{H^\pm} < 1 \text{ TeV}$ the only consequence, compared to our previous limits in Ref. [5], is the change of the absolute bound for IO, see Eq. (22).

We note, however, that for such large Yukawas, the pole mass calculation becomes numerically unstable in FlexibleSUSY and yields errors in the one-loop output for the sectors that are irrelevant for cLFV. However, the cLFV rates depend only on the Yukawa couplings and the $\overline{\text{MS}}$ charged Higgs mass m_{H^\pm} . The parameterization of Yukawa couplings of Eq. (5) is numerically stable and consistent with one-loop neutrino masses and mixings by construction, as was confirmed numerically. The cLFV observables are independent of the pole mass calculations up to the phase-space integration factor in FlexibleSUSY. This allows to speed up parameter scans by selecting the pole mass loop order setting to 0 in FlexibleSUSY LesHouches input.

Note, that this setting choice prints the pole masses and mixings inconsistent with the experimental data in the `FlexibleSUSY` output and hence they should be ignored for mentioned input option. We use the `FlexibleSUSY` extension `NPointFunctions` [20] to get three-body decay rates.

C. Perturbative unitarity bound

In the low scalar mass regime that was studied in [5], the bound on the Yukawa coupling that we got from two-body cLFV processes is strong enough, such that there was no need to care about bounds coming from perturbative unitarity. If the scalar mass m_{H^\pm} is larger, larger Yukawa couplings are in agreement with cLFV bounds and hence motivated. Since we are now covering the large scalar mass regions, we have to be more careful in order to be consistent with the perturbative unitarity constraints for Yukawa couplings. Using the bounds described in [21] and applying them to the GNM, we get the requirement:

$$\sum_i |Y_i^{(2)}|^2 < 8\pi. \quad (18)$$

Using Eq. (5), we can translate the unitarity bound Eq. (18) into a bound on Λ , which depends on z, ω_{22}, r :

$$\Lambda > \frac{m_2^{\text{pole}} f_z(r, \omega_{22})}{8\pi}, \quad (19)$$

$$f_z(r, \omega_{22}) = \frac{\cos^2 r + t_{32}^2 \sin^2 r}{z(r, \omega_{22})}.$$

For $|z| > 0.5$, we get the following ranges for Λ :

$$\begin{aligned} \text{NO: } \Lambda &> (0.34 - 6.1) \cdot 10^{-12} \text{ GeV}, \\ \text{IO: } \Lambda &> (1.2 - 4.6) \cdot 10^{-12} \text{ GeV}. \end{aligned} \quad (20)$$

For $\eta_2 = 0$ at two special points of interest, the perturbative unitarity bounds give:

$$\begin{aligned} \text{NO: } \Lambda &> 3.7 \cdot 10^{-12} \text{ GeV for } Y_e^{(2)} = 0, \\ &> 5.0 \cdot 10^{-13} \text{ GeV for } Y_\mu^{(2)} = 0, \\ \text{IO: } \Lambda &> 2.2 \cdot 10^{-12} \text{ GeV for } Y_e^{(2)} = 0, \\ &> 2.1 \cdot 10^{-12} \text{ GeV for } Y_\mu^{(2)} = 0. \end{aligned} \quad (21)$$

In [5], we got the absolute bound on the photon factor $|\Lambda| m_{H^\pm}^2$ from two-body decays of $O(10^{-6}) \text{ GeV}^3$ while the typical one is of $O(10^{-4}) \text{ GeV}^3$. Comparing it with Eq. (19), we see that the absolute bound starts to compete with the perturbative unitarity bound for $m_{H^\pm} > 1 \text{ TeV}$ while we typically should expect stronger bounds from cLFV up to $m_{H^\pm} \sim 10 \text{ TeV}$. Note that

such a large value for the Higgs mass here is problematic from the consistency of the scalar sector alone, hence it is safe to say, that typically we have stronger constraints from cLFV, period. For the previously defined special regions, however, the bound (18) becomes important for $m_{H^\pm} > 1 \text{ TeV}$ and thus needs to be taken into account.

III. PHENOMENOLOGICAL ANALYSIS

A. The dependence of absolute and typical bounds on Majorana phase (two-body decays)

We begin our phenomenological analysis by studying the impact of the Majorana phase η_2 . It influences the value of the Yukawa couplings in the $\omega_{22} - r$ plane. In particular, the points in the $\omega_{22} - r$ plane where $Y_{e,\mu}^{(2)} = 0$ vary as a function of η_2 as can be obtained analytically from Eq. (14).

As discussed before, in most of the parameter space the decay $\mu \rightarrow e\gamma$ provides the strongest constraint; however the most conservative (“absolute”) bound is obtained by considering the two special points where $Y_{e,\mu}^{(2)} = 0$ and where $\mu \rightarrow e\gamma$ becomes insensitive. Hence we focus here on the bounds derived from these special points and study their η_2 dependence. The results are shown in figure 1.

The blue dashed lines in figure 1 correspond to the special point where $Y_\mu^{(2)} = 0$ and which is only constrained by $\tau \rightarrow e\gamma$. For this special point, all values of the photon factor below the blue dashed line are excluded by $\tau \rightarrow e\gamma$ (the lower/upper blue dashed line corresponds to current/next phase as defined in table II). The yellow line corresponds to the small region with $Y_\mu^{(2)} \approx 0$ and whose boundary is defined by Eq. (15). Again, the photon factor values below the line are excluded by $\tau \rightarrow e\gamma$ in all of this region.

The red shaded area in figure 1 highlights all photon factor values below the lowest yellow line. This area is excluded already by the weakest possible constraint from the current phase experiments in all of the parameter space — hence it is absolutely excluded already at present. If the next phase of the experiments do not see a signal, this absolutely excluded area will move up to the upper yellow line.

Similarly, the black dashed lines correspond to the special point where $Y_e^{(2)} = 0$ and which is only constrained by $\tau \rightarrow \mu\gamma$. The green dashed lines correspond to the small region around this point, defined by Eq. (15). At this point/in this small region, all photon factor values below the respective lines are excluded by $\tau \rightarrow \mu\gamma$ but not by other observables (the lower lines correspond to current phase experiments, the upper lines to next phase experiments). The limit in this region is stronger than the absolute bound derived from the yellow dashed line.

The region above the upper green line cannot be excluded by τ decays even at next phase of the experiments,

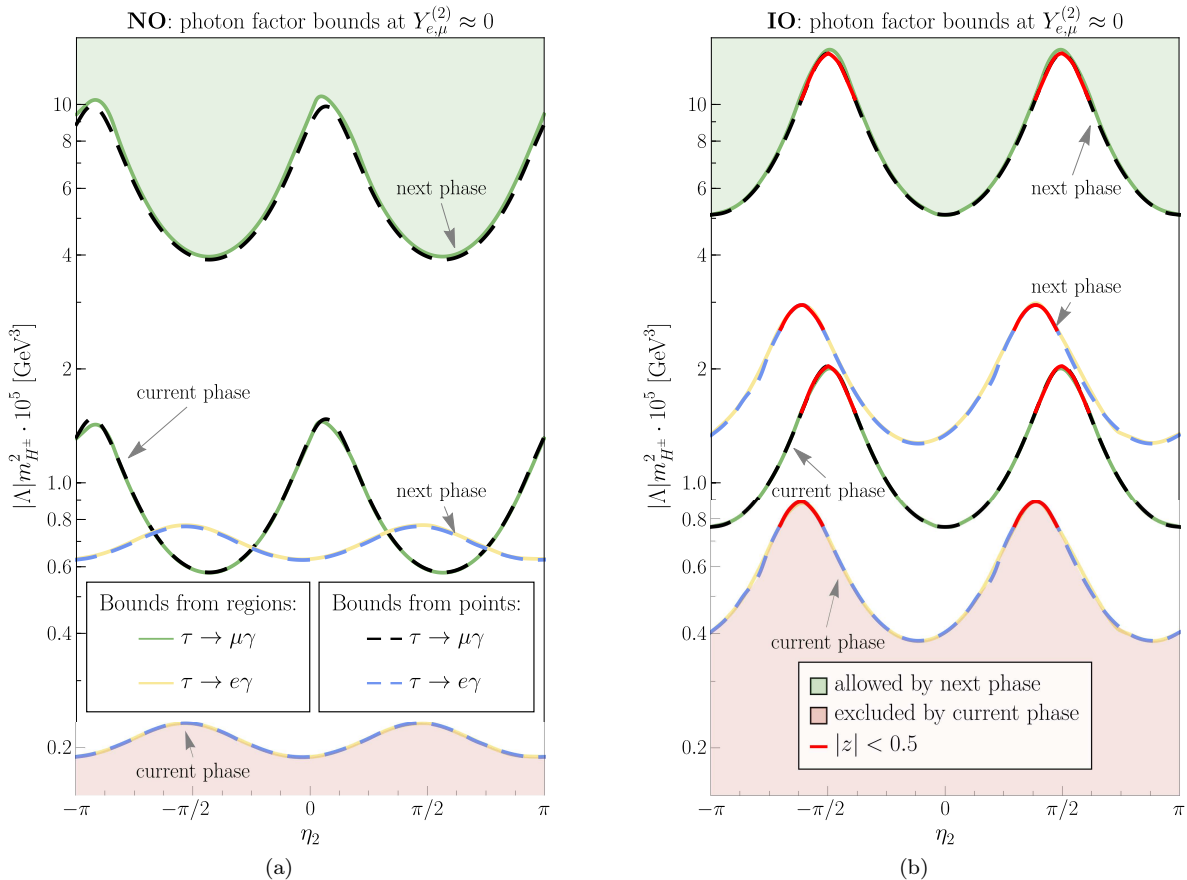


FIG. 1. Bounds on the photon factor $|\Lambda|m_{H^\pm}^2$ for two-body τ decays that come from the special points (extension of table 2 of Ref. [5]) and regions (extension of table 3 of Ref. [5]) for different Majorana phase η_2 values. The highest line corresponds to the special region and was defined as the *typical* limit. The lowest line comes from special points and corresponds to the weakest constraint of the GNM and was called *absolute* limit. Photon factors below the lines are excluded by the appropriate phase of the two-body decay experiments. This splits the whole area into three subregions: the red area is already excluded by current experiments (current phase from table II), the white area that can potentially be excluded by two-body decays of the planned experiments (next phase from table II) and the green region that will remain allowed by the limits on the two-body decay in the planned experiments. For IO special points can move into the parameter region in which $|z| < 0.5$ for specified ranges of η_2 (highlighted by the red color). There, $|z|$ varies in the following regions: for $Y_e^{(2)} = 0$ by $|z| \in (0.38, 0.48)$ and for $Y_\mu^{(2)} = 0$ by $|z| \in (0.43, 0.49)$.

given existing $\mu \rightarrow e\gamma$ constraints, however typically values of the photon factor close to the green/blue dashed lines are excluded by $\mu \rightarrow e\gamma$ — hence we refer to these lines as “typical” bounds. We refer to Ref. [5] for extensive discussions of absolute and typical bounds and for details on the $\mu \rightarrow e\gamma$ constraints on the entire parameter space.

Bounds on the photon factor derived from points $Y_{e,\mu}^{(2)} = 0$ and from small regions $Y_{e,\mu}^{(2)} \approx 0$, defined by Eq. (15) are almost the same, as seen in figure 1. The small difference in these bounds reflects the smallness of these regions. Thus from now on, we approximate the

bounds that come from special regions by the ones from special points.

Our main result here is the impact of the Majorana phase. Figure 1 shows that the dependence on η_2 value does not lead to a drastic change in the two-body decay bounds. The variation of the absolute bound is either roughly a factor of 1.25 for NO or a factor of 2 for IO. The absolute bound for $\eta_2 = 0$ is actually very close to the lowest possible value. Hence, the result for the absolute bound obtained in [5] remains indeed also the absolute lower bound if we include η_2 in the analysis as well.

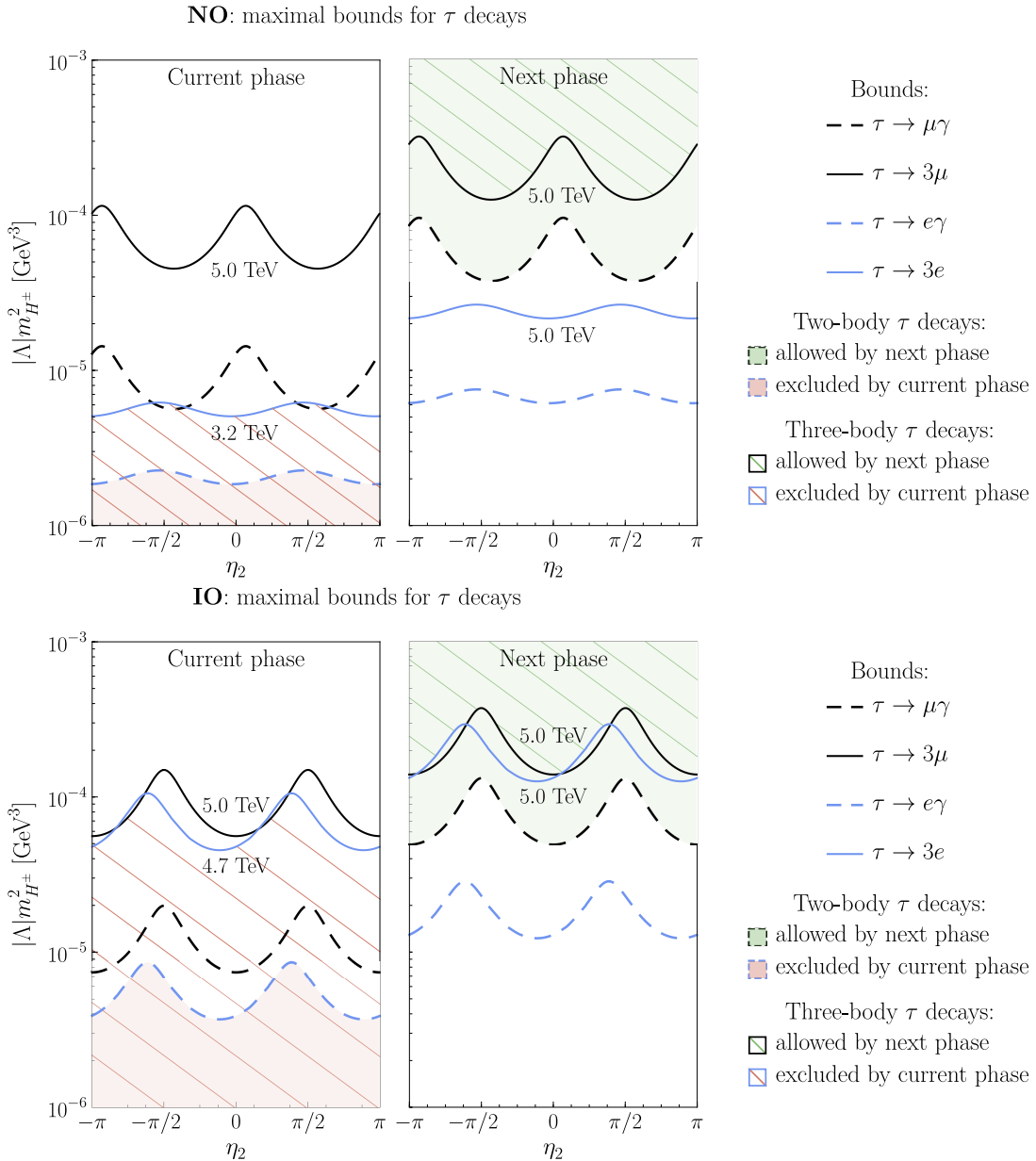


FIG. 2. Maximal bounds on the photon factor $|\Lambda|m_{H^\pm}^2$ for three-body τ decays that come from the special points for different Majorana phase η_2 values. Two-body decay bounds are shown for the comparison. In general, the limits defined by three-body decays depend on the value of m_{H^\pm} . Here, the highest possible lines for three-body decays are shown accompanied with the corresponding charged Higgs boson mass. The regions with $|z| < 0.5$ exist for three-body decays and are the same as in figure 1, however they are not shown here in order not to overcrowd the plot.

B. The importance of three-body decays

The three-body decays are expected to contribute significantly in regions of a large Higgs mass. There, for a fixed photon factor value, the box factor $\Lambda^2 m_{H^\pm}^2$ becomes smaller (equivalently, Λ becomes smaller and Yukawa couplings are enhanced), so that boxes are enhanced relatively to photonic diagrams. This enhancement might improve the limits that were obtained from two-body de-

cays alone. To illustrate this, we consider the same parameter scenarios as in figure 1 and look at maximum possible restrictions from the three-body decays, to see how figure 1 is modified. The results are shown in figure 2, where, in order not to overcrowd the pictures, we split bounds from current and next phases of experiments into separate subfigures.

The dashed lines are the same as in figure 1. They correspond to the constraints from $\tau \rightarrow e\gamma$ (for the specific

point with $Y_\mu^{(2)} = 0$) and from $\tau \rightarrow \mu\gamma$ (for the specific point with $Y_e^{(2)} = 0$). The new solid lines correspond to the additional limits from three-body decays ($\tau \rightarrow 3e$ for $Y_\mu^{(2)} = 0$ and $\tau \rightarrow 3\mu$ for $Y_e^{(2)} = 0$). These limits depend on m_{H^\pm} ; we have plotted the limits for specific values of m_{H^\pm} as indicated. These values are the maximum possible values for which the bounds, derived from the cLFV decays are still stronger than the perturbative unitarity bound.

From figure 2 we see that three-body decays can indeed lead to more severe bounds on $|\Lambda|m_{H^\pm}^2$. In fact, the absolute bound for large m_{H^\pm} is now defined by $\tau \rightarrow 3e$. The green (where τ decays are not expected at Belle-II) and the red (absolutely excluded) shaded regions are now also modified, as shown by hatching.

This highlights that the box amplitudes can change the picture significantly. However, we also see that the functional dependence on η_2 for $\ell \rightarrow \ell'\gamma$ and the corresponding $\ell \rightarrow 3\ell'$ are the same. Having that in mind, we will now set $\eta_2 = 0$ again, and study the competition between box and photonic contributions in more detail.

C. Absolute bounds from photon and box factors

Ref. [5] has shown that the cLFV amplitudes in the tiny seesaw parameter region are essentially governed by two quantities — the box factor $\Lambda^2 m_{H^\pm}^2$ (which was neglected in small m_{H^\pm} region) and the photon factor $|\Lambda|m_{H^\pm}^2$. The previous subsection has shown that the box contributions and three-body decays can be significant in the extended parameter region. Here we study the interplay of all these contributions in more detail. We study the constraints in the $\Lambda^2 m_{H^\pm}^2 - |\Lambda|m_{H^\pm}^2$ plane to see which contributions, which processes, or which constraints are more important in different parameter regions. We thus set $\eta_2 = 0$ and plot the constraints from both, two and three-body decays in the $\Lambda^2 m_{H^\pm}^2 - |\Lambda|m_{H^\pm}^2$ plane in figure 3. The plots in figure 3 contain a wealth of information which we explain step by step.

First, consider again the bounds from $\tau \rightarrow e\gamma$ for the specific point where $Y_\mu^{(2)} = 0$. The two-body decays do not depend on the box factor, thus the current/next phase constraints from $\tau \rightarrow e\gamma$ are seen as the horizontal blue dashed lines, as in figures 1 and 2. Similarly, the bounds from $\tau \rightarrow \mu\gamma$ for the point where $Y_e^{(2)} = 0$ are shown by the horizontal black dashed lines. The shaded areas between these dashed lines correspond to the white area in figure 1 at $\eta_2 = 0$. The absolutely excluded region for two-body decays (also shown as red area in figure 1) is below the lowest blue dashed line.

To understand the three body decays, consider, for example, the rightmost $\tau \rightarrow 3e$ blue solid line for which the decay rate is the same as the sensitivity in Belle-II. Going down this line from highest point to the lowest point corresponds to reducing the value of m_{H^\pm} . Go-

ing down, around $m_{H^\pm} \approx 400$ GeV, the curve starts to deviate more significantly from the vertical line and close to $m_{H^\pm} = 250$ GeV the curve becomes horizontal. This means that around those masses, the box contributions become negligible and photonic diagrams dominate. One can see that all the constraints from $\tau \rightarrow 3e$ and $\tau \rightarrow 3\mu$, wherever they are allowed by the two-body decays (higher than the corresponding dashed lines) are almost vertical. This indicates the box dominance of the three-body decays.

For NO the region between the blue lines (for $\tau \rightarrow e\gamma$, $\tau \rightarrow 3e$ and the point with $Y_\mu^{(2)} = 0$) does not overlap with the region between the black lines (for $\tau \rightarrow \mu\gamma$, $\tau \rightarrow 3\mu$ and the point with $Y_e^{(2)} = 0$). For IO the corresponding region in the $\Lambda^2 m_{H^\pm}^2 - |\Lambda|m_{H^\pm}^2$ plane overlap significantly. This is in line with figure 1 (at $\eta_2 = 0$). This figure also shows that the relative overlap between these regions would change for other values of η_2 .

The perturbative unitarity limit on Λ of Eq. (19) can be applied to the special points where $Y_{\mu,e}^{(2)} = 0$. This results in the left borders of the blue/black shaded regions given by the contour lines of the indicated values of Λ . The existence of these borders means e.g. that the unitarity limit becomes stronger than the one coming from $\tau \rightarrow 3e$ in certain parameter regions. With the help of the contour lines for fixed mass m_{H^\pm} , one can see that for the current experimental limits (current phase) this happens around $m_{H^\pm} \approx 3.2(4.7)$ TeV, which is consistent with the value shown in figure 2. In other cases, next phase experiments put stronger bounds than the perturbative unitarity limit, as the heaviest mass of the scanned values is reached.

To exemplify and highlight the interplay between two- and three-body decay bounds, we focus again on the special point with $Y_\mu^{(2)} = 0$, which leads to the most conservative, absolute bounds valid in all of the parameter space. The green and yellow shadings in figure 3 represent the allowed regions at $Y_\mu^{(2)} = 0$. The green region is allowed by current phase experiments but will be excluded by next phase experiments; the yellow regions will remain allowed if next phase experiments do not find a signal. For small charged Higgs masses, the regions are bounded from below by the horizontal blue dashed lines corresponding to the two-body decay $\tau \rightarrow e\gamma$. If the mass is increased, then at some value the bound from three-body decays ($\tau \rightarrow 3e$ in this case, solid blue line) becomes more restrictive. At even higher mass values, the perturbative unitarity can imply another type of restriction. However, only in the green region for current phase experiments this restriction is stronger than the one from the experimental constraints. The next phase experimental sensitivities give a stronger bound than the perturbative unitarity bound in all of the yellow region.

From the green and yellow areas in figure 3 one can infer at which m_{H^\pm} value the three-body decays become more important than the corresponding two-body ones. This also allows to update and generalize the limits from

cLFV obtained in [5]. The most conservative, “absolute” limits, at the point with $Y_\mu^{(2)} = 0$ are (for NO and IO):

$$\begin{aligned}
|\Lambda| m_{H^\pm}^2 &> 1.9(4.0) \cdot 10^{-6} \text{ GeV}^3 \\
&\text{with } m_{H^\pm} < 1.2(0.4) \text{ TeV}, \\
\Lambda^2 m_{H^\pm}^2 &> 2.6(98.7) \cdot 10^{-18} \text{ GeV}^4 \\
&\text{with } m_{H^\pm} \in 1.2 \div 3.2(0.4 \div 4.7) \text{ TeV}, \\
|\Lambda| &> 0.5(2.1) \cdot 10^{-12} \text{ GeV} \\
&\text{with } m_{H^\pm} > 3.2(4.7) \text{ TeV}.
\end{aligned} \tag{22}$$

The first line of Eq. (22) corresponds to $\tau \rightarrow e\gamma$, the second line to $\tau \rightarrow 3e$ and the last to the perturbative unitarity bound. The first line of Eq. (22) also corresponds to the limits in Ref. [5]. For IO the limit is modified. This comes from allowing larger Yukawa couplings and hence excluding lower Higgs masses, when we want to exclude all the Yukawa couplings, as discussed in section II B.

The region bordered by the upper black (solid and dashed) lines corresponds to the maximum region where cLFV τ decays might be observed at the next phase experiments. Above that region a large part of parameter space for generic values of Yukawa couplings can still be excluded by cLFV muon decays; hence these boundaries are referred to as “typical limits”. These typical limits are not affected by unitarity, and reading off from the $\tau \rightarrow \mu\gamma$ and $\tau \rightarrow 3\mu$ next phase experiment lines we ob-

D. Global box dominance of $\mu \rightarrow 3e$ ($\eta_2 = 0$)

Now we focus our attention on the more generic parameter space outside the special parameter points where $Y_{\mu,e}^{(2)} = 0$. Here the limits from cLFV muon decays are stronger and τ decays cannot be observed at next phase experiments. In this parameter region the interplay between the two-body decay $\mu \rightarrow e\gamma$ and the three-body decay $\mu \rightarrow 3e$ is of interest. We abbreviate:

$$R \equiv \frac{\text{BR}(\mu \rightarrow 3e)}{\text{BR}(\mu \rightarrow e\gamma)}. \tag{24}$$

For the low Higgs masses studied in [4], the relation between these two observables is simply fixed by the photon

dominance for NO (and IO):

$$\begin{aligned}
|\Lambda| m_{H^\pm}^2 &> 8.8(4.9) \cdot 10^{-5} \text{ GeV}^3 \\
&\text{with } m_{H^\pm} < 1.5(1.7) \text{ TeV}, \\
\Lambda^2 m_{H^\pm}^2 &> 3.4(0.85) \cdot 10^{-15} \text{ GeV}^4 \\
&\text{with } m_{H^\pm} > 1.5(1.7) \text{ TeV}.
\end{aligned} \tag{23}$$

These limits update the typical limits found in [5].

Finally, figure 3 also shows the parameter areas where an observation of *only* three-body decays is possible by next phase experiments while two-body decays are not observed. We discuss them only for the left panel of figure 3a for NO, where they are more straightforward to localize. The area denoted with the label “a” is above the upper dashed blue line, i.e. $\tau \rightarrow e\gamma$ cannot be observed at next phase experiments. However, it is to the left of the solid blue line still, hence $\tau \rightarrow 3e$ is still allowed. Hence this “a” area corresponds indeed to the case where $\tau \rightarrow 3e$ is observed and $\tau \rightarrow e\gamma$ is not in forthcoming experiments. Similarly, the area marked by “c” lies above the upper black dashed line and to the left of the solid black line. In this area $\tau \rightarrow 3\mu$ can be observed in the next phase experiments but $\tau \rightarrow \mu\gamma$ cannot. Also, near to $Y_\mu^{(2)} \approx 0$ (for both orderings), as was mentioned in the Ref. [5], there is a slight deviation from dipole dominance for $\mu \rightarrow 3e$. Together with the ratio between MEG-II and Mu3e-I experimental bounds, this allows to observe $\mu \rightarrow 3e$ while $\mu \rightarrow e\gamma$ is not seen. The allowed parameter region is marked “b” and is bordered by the red dashed line. It is also possible to observe $\mu \rightarrow 3e$ and $\tau \rightarrow 3e$ in the same time due to the aforementioned localization in the $\omega_{22} - r$ plane, while $\mu \rightarrow 3e$ and $\tau \rightarrow 3\mu$ cannot be detected at the same time in the GNM for the tiny seesaw regime. The drastic improvement of the sensitivity in Mu3e-II will make $\mu \rightarrow 3e$ observation possible in all the yellow region of figure 3 with photon dominated contributions for both orderings.

dominance:¹

$$\begin{aligned}
R \approx R_{\text{ph. dom.}} &\equiv -\frac{5\alpha}{18\pi} + \frac{\alpha}{3\pi} \left(\ln \frac{m_e^2}{m_\mu^2} - \frac{11}{4} \right) \approx 0.0059 \\
&\text{for } m_{H^\pm} < 1 \text{ TeV}.
\end{aligned} \tag{25}$$

Note, that the branching ratios for three-body decays are dominated by photonic contributions in the case of light m_{H^\pm} , while others — boxes, Z and Higgs penguins —

¹ In the published version of [5], there is a missing overall factor of $1/\pi$ in Eq. (5.1) for the expression of the photon dominance, see also e.g. Eq. (29) of [6] for the case of dipole dominance. This misprint does not affect any of the results presented in [5] or here.

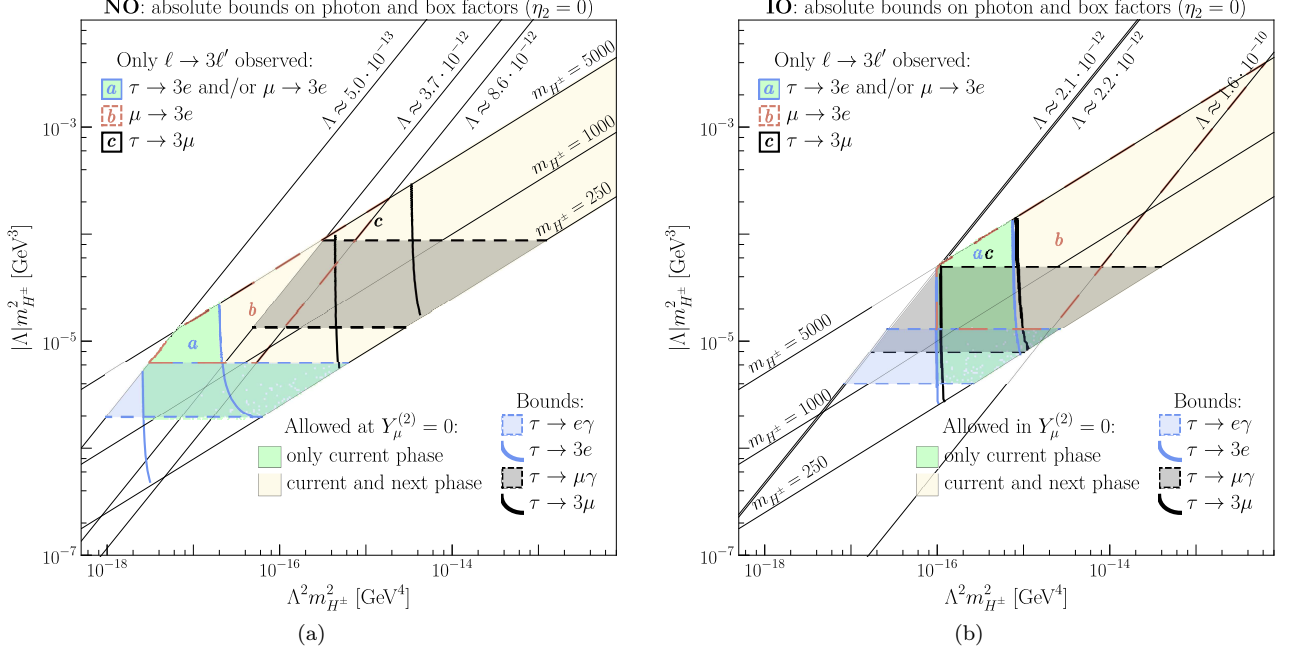


FIG. 3. Constraints from cLFV shown in the $\Lambda^2 m_{H^\pm}^2 - |\Lambda| m_{H^\pm}^2$ plane for $\eta_2 = 0$. Blue/black dashed and solid lines show the constraints of $|\Lambda| m_{H^\pm}^2$ and $\Lambda^2 m_{H^\pm}^2$ from current phase and next phase experiments at the parameter points $Y_\mu^{(2)} = 0/Y_e^{(2)} = 0$. The areas, named by letters, are the areas in which the three-body decays can be observed in the next phase experiments. The rightmost Λ values in both plots correspond to the limiting value for which the $\mu \rightarrow 3e$ in Mu3e-I can still be observed. The other shown Λ values are the same as in Eq. (21) and thus give perturbative unitarity constraints at each of the special points (lower Λ are excluded).

are negligible. This regime is called *photon* dominance as it is different from dipole dominance by additional non-negligible vector photon amplitudes, see [5]. However, this is no longer the case for the extended charged Higgs mass range considered here, and thus the ratio between these two observables can be different.

We plot the possible ratios of $\mu \rightarrow 3e/\mu \rightarrow e\gamma$ for fixed $\text{BR}(\mu \rightarrow e\gamma)$ at current limits (normalized to the photon dominance value) for different photon factor values in figure 4. The colors for photon factor values are consistent with the coloring scheme of figure 6 of Ref. [5] and correspond to the same regions in $\omega_{22} - r$ plane of that reference. The very highest values (darkest blue) come from a region close to the special region, in which $Y_\mu^{(2)} \approx 0$. This can be easily understood by recalling that photonic amplitudes are proportional to $Y_\mu^{(2)} Y_e^{(2)}$, while boxes $\propto Y_\mu^{(2)} (Y_e^{(2)})^3$, thus the photonic contribu-

tions are suppressed relative to the box ones. Getting further away from this region, we get lower and lower box enhancement. The regions close to $Y_e^{(2)} \approx 0$ have box contributions suppressed, thus correspond to photon dominance. They also correspond to a smaller photon factor value (of dark blue). However, they are not visible in figure 4 as they are hidden behind the largest parameter space with high photon factor value (orange).

In general, the deviations from photon dominance are caused by large Yukawa couplings which in turn are correlated with small Λ , see Eq. (5). In figure 4, therefore, small photon factor and/or large charged Higgs mass correlates with strong deviations from photon dominance, as can be seen from Eq. (17). For example, outside the darkest blue region with photon factor less than 10^{-4} , deviations from photon dominance by a factor of two can be reached if the charged Higgs mass is above 3 TeV.

E. Yukawa “fingerprint” of the model ($\eta_2 = 0$)

So far we have employed the advantageous parameterization of Yukawa couplings in terms of the $\omega_{22} - r$ plane. Now we finally show how the model constrains affect the actual values of the Yukawa couplings $Y^{(2)}$. Since these

are the fundamental Lagrangian parameters, constraints on them are of interest since they might shed light on possible patterns and fundamental origins of the Yukawa couplings.

More specifically, we look at the minimum vs. maximum values of the components of the three-vector $Y^{(2)}$

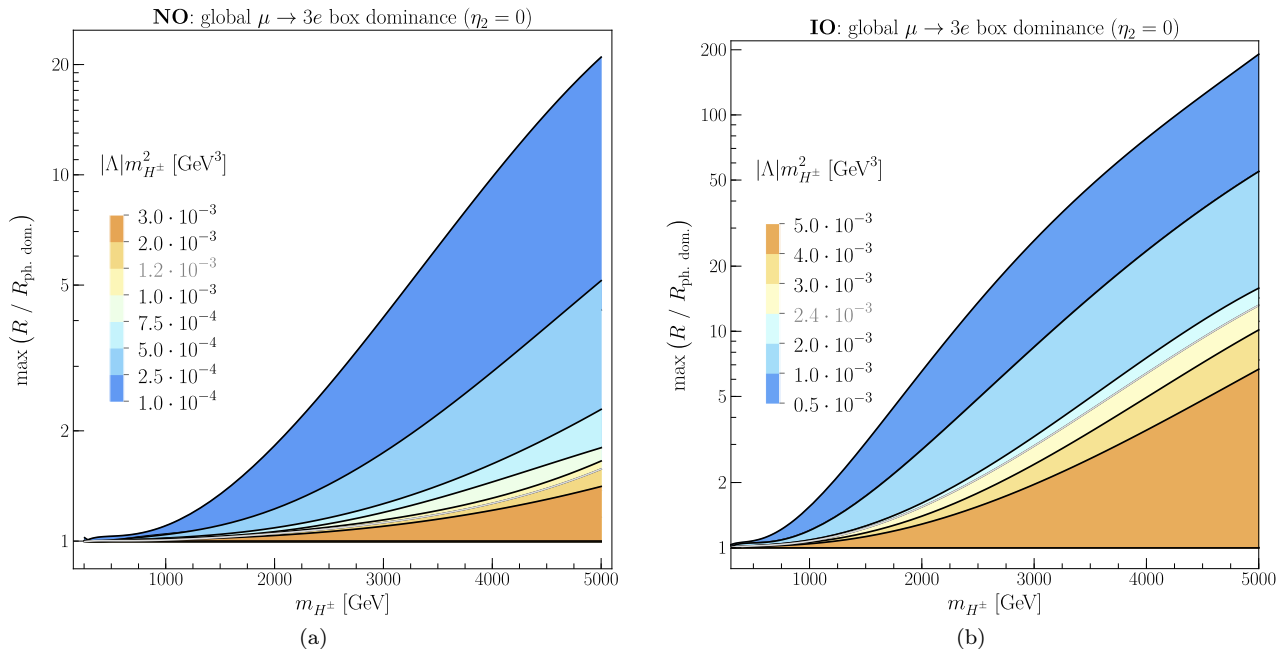


FIG. 4. Maximal currently allowed deviation from photon dominance as a function of m_{H^\pm} in the typical parameter region. It is plotted as a maximal currently allowed ratio of $R \equiv \text{BR}(\mu \rightarrow 3e)/\text{BR}(\mu \rightarrow e\gamma)$, normalized to the ratio $R_{\text{ph. dom.}}$, calculated from Eq. (25), i.e. when the photon dominance is assumed. Colors show photon factor values for which these deviations can occur.

as a two-dimensional scatter plot. In this way we show which overall magnitudes of Yukawa couplings are possible, and also whether the Yukawa couplings can/should involve strong hierarchies or not.

The resulting plot is given in figure 5. Every point in the plot corresponds to a bin of Yukawa values, while other parameters are scanned over, see Eq. (13). Different colors correspond to allowance/exclusions of current/next phases of experiments, which could be captured by a scan in the parameter space. The diagonal lines separate the orders of magnitude of hierarchies between the Yukawa couplings. For instance, the very lowest diagonal line corresponds to the case, in which all the components of $Y^{(2)}$ are equal, while the leftmost corresponds to the $O(10^3)$ ratio between the minimum and maximum value of $Y^{(2)}$. The special points with $Y_{\mu,e}^{(2)} = 0$ discussed in previous subsections would be located to the left of the visible plot range in figure 5.

The dark red region in figure 5 is excluded already by current phase experiments. In this completely excluded

region the Yukawa couplings take rather large values; everywhere in the dark red region at least one Yukawa coupling is above 0.1.

The dark green region is experimentally allowed and will remain allowed even if next phase experiments see no signal. As expected this region contains smaller Yukawa couplings; though non-hierarchical Yukawa couplings are possible up to values of 10^{-2} and hierarchical Yukawa couplings are possible where the minimum/maximum Yukawa values are around $10^{-3} \div 1$. The yellow region, and the regions with different lighter shadings of yellow and red, are *ambiguous*. Each bin in these regions contains points which are allowed now by current phase experiments and points which can be excluded by next phase experiments, as explained in the legend of the figure. This region is thus the region which will be scrutinized by next phase experiments, and part of this region can be excluded. In the yellow region there exist parameter points where all Yukawa couplings are $\mathcal{O}(0.1)$ as well as hierarchical points where the minimum/maximum Yukawa coupling values are around $10^{-3} \div 1$.

IV. CONCLUSIONS

We completed the cLFV study of the GNM by investigating its full parameter space. The enlarged parameter space, compared to the previous study [5], is summarized

in table III. The GNM remains a favorable explanation of neutrino masses in the parameter region of tiny seesaw scale, i.e. a seesaw scale below the electroweak scale. In addition, this leads to a prediction of two- and three-body decay cLFV processes and provides reasonable re-

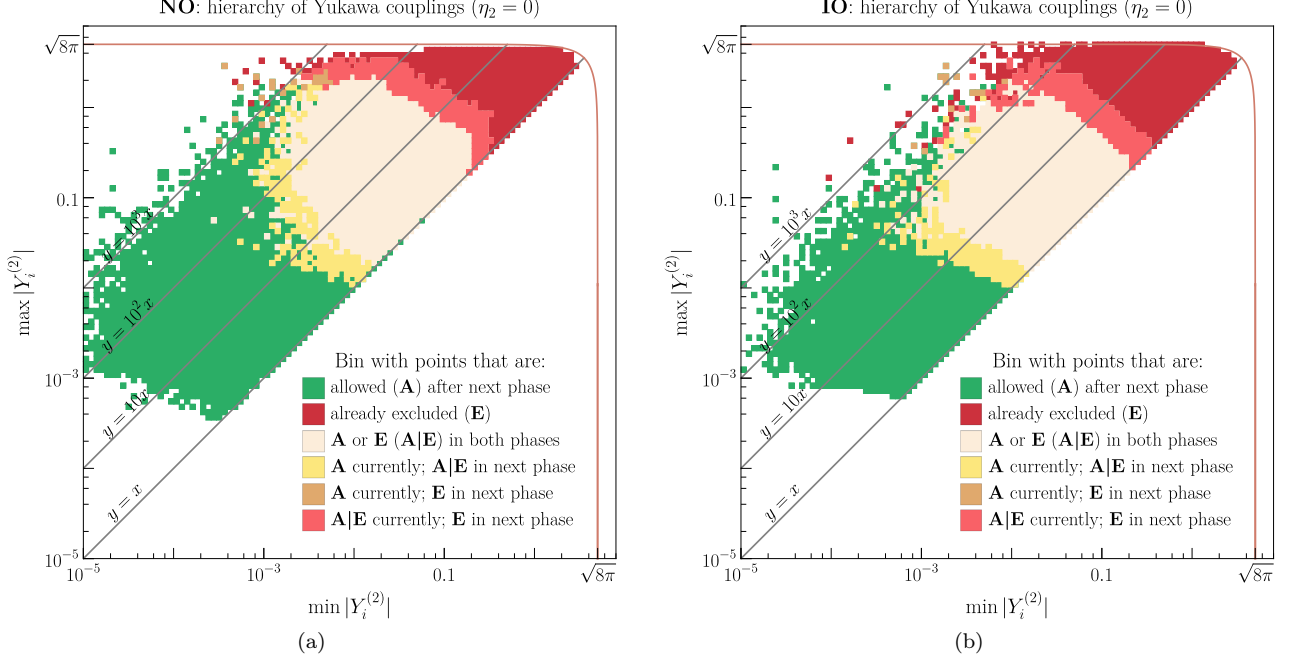


FIG. 5. Constrains on Yukawa couplings from cLFV. The Yukawa couplings, which are always allowed, sometimes allowed (depending on other variables), and always excluded by both current and next phase experiments are colored by green, yellow and red respectively. The regions, which change from “allowed” to “ambiguous” and from “ambiguous” to “excluded” after next phase experiments are indicated by more intensive yellow and red colors.

restrictions on the scalar and leptonic parameters.

Just as in the previous study, the weakest and the most conservative (“absolute”) bounds on the photon factor are provided by τ two- and three-body decays in special regions in which one of the Yukawa couplings vanishes $Y_{e,\mu}^{(2)} \approx 0$. The impact of the Majorana phase η_2 can be seen in figure 1. It does not lead to a drastic change in the two-body decay bounds, i.e. the bounds stay within an order of magnitude as a function of η_2 . Also, the absolute bound for $\eta_2 = 0$ turns out to be very close to the lowest possible value. This means that the result for the absolute bound obtained in [5] remains the absolute lower bound for general η_2 to a very good approximation.

In the parameter regions with m_{H^\pm} above the TeV scale, larger Yukawa couplings are possible, see figure 2. As a result, box diagram contributions governed by four powers of Yukawa couplings dominate the three-body decay observables, in contrast to the photonic dominance for the low-mass region. For high m_{H^\pm} and in the special regions ($Y_{e,\mu}^{(2)} \approx 0$), perturbative unitarity constraints for Yukawa couplings, Eq. (18), can become more relevant than cLFV ones.

Figure 3 summarizes the main constraints for $\eta_2 = 0$, which are the restrictions in the $\Lambda^2 m_{H^\pm}^2 - |\Lambda| m_{H^\pm}^2$ plane from both two and three-body decays. The figure shows that the parameter space is constrained by an interplay between box-dominated three-body decays, two-body decays, and perturbative unitarity. Thus we update the absolute and typical bounds in Eq. (22) and in Eq. (23).

Outside of the special regions where specific Yukawa couplings vanish and where τ decays are important, $\mu \rightarrow e\gamma$ still restricts the majority of the parameter space due to stronger experimental bounds. Also, complementary to this two-body decay, $\mu \rightarrow 3e$ will become competitive already in the next phase (Mu3e-I) and will become even more restrictive at Mu3e-II. In addition to the purely experimental arguments mentioned above, the latter observable is affected by the box contributions that are enhanced for larger values of m_{H^\pm} . This allows for significant deviations from photon dominance, which are shown in figure 4 for Mu3e-I.

We recall that the scoto-seesaw model and the GNM in the tiny seesaw scale have the same predictions for cLFV and thus all our results are directly applicable for a scoto-seesaw model, too. One should expect the same qualitative behavior for the scotogenic model in these parameter regions, as argued in [5]. Thus by studying the GNM, we also complement the previous studies of cLFV of scoto-seesaw and scotogenic models by including the tiny sterile neutrino mass region.

ACKNOWLEDGMENTS

U.Kh. was supported by the Deutscher Akademischer Austauschdienst (DAAD) under Research Grants — Doctoral Programmes in Germany, 2019/20 (57440921) and by the DFG under grant number STO 876/7-1. W.K.

was supported by the National Science Centre (Poland) under the research grant 2020/38/E/ST2/00126. V.D.

and T.G. thank the Lithuanian Academy of Sciences for their support via project DaFi2021.

-
- [1] E. Ma, Phys. Rev. D **73**, 077301 (2006), arXiv:hep-ph/0601225.
- [2] N. Rojas, R. Srivastava, and J. W. F. Valle, Phys. Lett. B **789**, 132 (2019), arXiv:1807.11447 [hep-ph].
- [3] W. Grimus and H. Neufeld, Nucl. Phys. B **325**, 18 (1989).
- [4] V. Dūdėnas and T. Gajdosik, Acta Phys. Polon. Supp. **15**, 1 (2022).
- [5] V. Dūdėnas, T. Gajdosik, U. Khasianeich, W. Kotlarski, and D. Stöckinger, JHEP **09**, 174, arXiv:2206.00661 [hep-ph].
- [6] T. Toma and A. Vicente, JHEP **01**, 160, arXiv:1312.2840 [hep-ph].
- [7] A. Vicente and C. E. Yaguna, JHEP **02**, 144, arXiv:1412.2545 [hep-ph].
- [8] S. Mandal, R. Srivastava, and J. W. F. Valle, Phys. Lett. B **819**, 136458 (2021), arXiv:2104.13401 [hep-ph].
- [9] P. Zyla *et al.* (Particle Data Group), PTEP **2020**, 083C01 (2020).
- [10] A. M. Baldini *et al.* (MEG), Eur. Phys. J. C **80**, 858 (2020), arXiv:2005.00339 [hep-ex].
- [11] A. M. Baldini *et al.* (MEG II), Eur. Phys. J. C **78**, 380 (2018), arXiv:1801.04688 [physics.ins-det].
- [12] B. Aubert *et al.* (BaBar), Phys. Rev. Lett. **104**, 021802 (2010), arXiv:0908.2381 [hep-ex].
- [13] W. Altmannshofer *et al.* (Belle-II), PTEP **2019**, 123C01 (2019), [Erratum: PTEP 2020, 029201 (2020)], arXiv:1808.10567 [hep-ex].
- [14] U. Bellgardt *et al.* (SINDRUM), Nucl. Phys. B **299**, 1 (1988).
- [15] A. Wasili (Mu3E), PoS **ICHEP2020**, 898 (2021).
- [16] K. Hayasaka *et al.*, Phys. Lett. B **687**, 139 (2010), arXiv:1001.3221 [hep-ex].
- [17] P. Athron, J.-h. Park, D. Stöckinger, and A. Voigt, Comput. Phys. Commun. **190**, 139 (2015), arXiv:1406.2319 [hep-ph].
- [18] P. Athron, M. Bach, D. Harries, T. Kwasnitza, J.-h. Park, D. Stöckinger, A. Voigt, and J. Ziebell, Comput. Phys. Commun. **230**, 145 (2018), arXiv:1710.03760 [hep-ph].
- [19] P. Athron, A. Büchner, D. Harries, W. Kotlarski, D. Stöckinger, and A. Voigt, Comput. Phys. Commun. **283**, 108584 (2023), arXiv:2106.05038 [hep-ph].
- [20] U. Khasianeich, W. Kotlarski, and D. Stöckinger, in *Computational Tools for High Energy Physics and Cosmology* (2022) arXiv:2206.00745 [hep-ph].
- [21] L. Allwicher, P. Arnan, D. Barducci, and M. Nardecchia, JHEP **10**, 129, arXiv:2108.00013 [hep-ph].